Int j simul model 21 (2022) 4, 567-578
Original scientific paper

ON THE CHOICE OF THE NUMERICAL CONTACT STIFFNESS PARAMETER FOR THE MODAL ANALYSIS

Wittmann, J.; Hüter, F.; Zahn, A.; Tremmel, S. & Rieg, F.
Faculty of Engineering Science, University of Bayreuth,
Universitätsstraße 30, 95447 Bayreuth, Germany
E-Mail: johannes.wittmann@uni-bayreuth.de, florian.hueter@uni-bayreuth.de,
aljoscha.zahn@gmail.com, stephan.tremmel@uni-bayreuth.de, frank.rieg@uni-bayreuth.de

Abstract

Modal analysis carried out within the Finite-Element-Analysis leads to natural frequencies and mode shapes. Using adjacent solids in linear dynamics generates a computational contact problem with several configuration parameters. Contact stiffness is of importance as it affects the accuracy and convergence behaviour of the results. Thus, an overlarge value leads to a locking phenomenon and causes ill-conditioned system matrices. This paper investigates whether recommendations for appropriate contact stiffnesses in static mechanics are also applicable to modal analysis. In fact, it can be observed that a significantly smaller contact stiffness than stated in the literature is also well suited for modal analysis. Furthermore, choosing the optimum range for the numerical contact stiffness for modal analysis depends on the order of the natural frequency and the corresponding vibration mode. The results of the simulations are validated against experimental modal analysis of a sample with identical elastic properties. The verified contact settings in the present paper permit a more realistic consideration of contact constraints in modal analysis.

(Received in June 2022, accepted in September 2022. This paper was with the authors 2 weeks for 1 revision.)

Key Words: Finite-Element Modal Analysis, Computational Contact Mechanics, Contact Stiffness, Experimental Modal Analysis

1. INTRODUCTION

In many applications of drivetrain technology, Finite-Element-Analysis (FEA) is a proven tool to receive information about characteristics of structural dynamics. External forces and attenuation are challenging to investigate and often approximated for implicit transient analysis. Quite frequently, engineers underestimate the associated disadvantages like high computation time and storage in time-domain simulations. In such cases, the modal analysis in operating points may be helpful to capture dynamic parameters like mode shapes and natural frequencies of prototypes in a quick first attempt [1, 2].

When two or more solids are combined in a simulation with non-matching meshes, a valid result can be obtained using contact analysis. Following the main principle, the contact mechanics represent a non-linearity in the simulation [3]. Thus, a basic assumption for modal analysis is that we deal with linear primary states in contrast to the non-linear, transient analysis. For instance, the closed contact is presumed in this short operating state as linear, not changing over the modal analysis duration.

Contact definition allows us to classify constraints with normal and tangential contact stiffness parameters and different types of contact discretization. Most prior research has investigated appropriate contact settings, especially for the static FEA and topology optimization. According to Billenstein et al. [4] so-called contact stiffness supports occur, which have a significant and negative influence on the simulation results. Therefore, some criteria for suitable contact parameters are provided by the literature in order to obtain correct solutions. So far, comparatively few contributions link contact settings with modal analysis. For this reason, advanced specifications for the contact stiffness are needed in natural vibration analysis. In this research, only the stiffness terms and not inertia terms are imposed with contact

https://doi.org/10.2507/IJSIMM21-4-616

constraints. Consequently, the research question refers to the influence of the numerical contact stiffness on the natural frequencies and their mode shapes. If we take excessive contact stiffness parameters as an example, increased natural frequencies and manipulated mode shapes appear as wrong results. This effect is intensified by gradually refined meshes that contain big element volume differences. Therefore, the present paper aims to provide helpful guidance for selecting suitable contact settings to calculate correct eigenvalues and eigenvectors. In addition to this, the influence of inappropriate contact stiffnesses on the natural frequencies and mode shapes is shown. A flat steel clamped on one side serves as a demonstrator. The FEA model consists of a non-matching and locally refined mesh, where the contact zone is located in the middle of the thickness direction (see Fig. 5). A structured fine mesh without a contact zone is used for comparison of the investigations. The experimental modal analysis (EMA) of a single steel part with identical elastic behaviour as in the simulations provides a reference to verify the simulations of different numerical contact settings.

2. CONTACT DYNAMICS IN MODAL ANALYSIS

2.1 Undamped modal analysis

The paper begins by clarifying the methods in computational contact dynamics, which are required to investigate the contact stiffness. The undamped equilibrium equations consist of inertia and stiffness as well as external forces and represent the linear differential equation [5]:

$$\boldsymbol{Ku} + \boldsymbol{M\ddot{u}} = \boldsymbol{f} \tag{1}$$

Without considering damping forces for the modal analysis, the balance of powers arises from multiplying the displacement vector $\boldsymbol{u}$ by the stiffness matrix $\boldsymbol{K}$ and the acceleration vector $\boldsymbol{\ddot{u}}$ by the mass matrix $\boldsymbol{M}$. Without external forces $\boldsymbol{f}$ and by taking a special solution function $\boldsymbol{u} = \boldsymbol{\varphi} e^{i\omega t}$ into account [5], Eq. (1) becomes the generalized eigenvalue problem:

$$\left(\boldsymbol{K} - \omega_i^2 \boldsymbol{M}\right)\boldsymbol{\varphi}_i = \boldsymbol{0} \tag{2}$$

Solving Eq. (2) returns $n = dim(\boldsymbol{K})$ eigenvalues $\Lambda_i = \omega_i^2$ with the corresponding eigenvectors $\boldsymbol{\varphi}_i$. All solutions can be written in a mode shape matrix $\boldsymbol{\Phi}$ and the eigenvalue matrix $\boldsymbol{\Lambda}$ [5]:

$$\boldsymbol{\Phi} = [\boldsymbol{\varphi}_1, \boldsymbol{\varphi}_2, \ldots, \boldsymbol{\varphi}_n] \tag{3}$$

$$\boldsymbol{\Lambda} = \begin{bmatrix} \omega_1^2 & 0 & \cdots & 0 \\ 0 & \omega_2^2 & \vdots & 0 \\ \vdots & \cdots & \ddots & \vdots \\ 0 & 0 & \cdots & \omega_n^2 \end{bmatrix} \tag{4}$$

The natural frequencies f_i result by dividing the angular frequencies ω_i by 2π radians. In many technical applications, only the first few eigenvalues are of interest, as higher-order frequencies are seldom in the critical range. So the number of eigenvalues of interest $k \ll n$ is small in comparison to the dimension of the equation system n. This is due to the fact that, in general, only the low orders of the natural frequencies are technically relevant. In our case the results are calculated for the first six natural frequencies and the corresponding mode shapes. Therefore, iterative procedures solve the eigenproblem with the reduced dimension k of a mathematically equivalent structure to Eq. (2) [6]. Most common methods for solving eigenproblems are the subspace iteration and the Lanczos algorithm [5-7]. Another solution method is given by the Arpack library to solve large scale eigenvalue problems [8]. It is based on a reverse communication interface, which requires an external matrix-vector-operation solver in an implicitly restarted Arnoldi method. In Arpack, extremal eigenvalues with large magnitudes are generally easier and faster to calculate than small eigenvalues. The shift-invert mode is for that reason the possibility to get smallest natural frequencies and eigenvectors with an efficient performance. Accordingly, Eq. (2) has to be transformed [8] into an extended eigenvalue problem:

$$(\boldsymbol{K} - \sigma \boldsymbol{M})^{-1} \boldsymbol{M} \boldsymbol{\varphi}_i = \nu \boldsymbol{\varphi}_i \tag{5}$$

where:

$$\nu = (\omega_i^2 - \sigma)^{-1} \tag{6}$$

A high convergence is provided for the solution of eigenvalues near to σ with this shift and invert spectral transformation [8]. The shift value of our analyses is $\sigma = 0$, so the first six smallest eigenfrequencies are calculated.

2.2 Contact dynamics

In FEA, the interaction between solids is based on the contact analysis. A non-matching mesh commonly leads to the contact search based on the master-slave-concept [4, 9]. One possibility to realize the contact after successfully detecting the contact pairs is the Node-to-Segment (NTS) discretization [9, 10]. For instance, nodes of the slave solid get connected with an element-facet from the master solid, see Fig. 1 a. Another possible method is an extension of the NTS contact discretization. The focus here is on the use of integration points of element facets from the slave solid, see Fig. 1 b, [9-12]. These can be interpolation points like Gauss points instead of discrete nodes. If hexahedral segments are considered, then one, four or sixteen contact points are typically available [9].

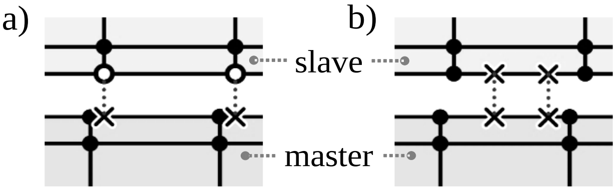

Figure 1: Contact discretization, regarding a) Node-to-Segment and b) Gauss-Point-to-Segment [4].

In a next step a geometric contact condition is needed for each contact pair. Constraints formulate the restrictions on the finite element model. In general, they are distinguished into normal and tangential directions with respect to the solid surfaces [4, 13]. Three possible gap conditions g between the slave and the master coordinates are defined [14]: no contact ($g > 0$), ideal contact ($g = 0$) and penetration ($g < 0$, inadmissible). For the special case of bonded contact type (tied), all contact forces and displacements in tangential and normal direction are transmitted equally. Therefore, a distinction into the directions is not necessary for the constraints, respectively, for a basic solvability of the bonded contact [9]. Subsequently, the kinematic constraints [15] are used to extend the system stiffness with a contact constraint matrix:

$$\boldsymbol{G}\boldsymbol{u} = \boldsymbol{v} \tag{7}$$

For all active constraints, the coefficients are contained in $\boldsymbol{G}$ and the corresponding right-hand side vector $\boldsymbol{v}$ includes the restrictions [4]. These restrictions affect the structure, like in this matter as initial contact distances.

There are a number of established methods to consider constraints of Eq. (7) within the FE problem of Eq. (2) like the perturbed Lagrange- and the penalty method. Furthermore, in structural dynamics it is also conceivable to implement the standard mass penalty and bipenalty formulations [16, 17]. In contrast, the effort for the modal analysis can be reduced if only stiffness and not additionally mass is subjected to contact conditions [18]. With these assumptions, Eq. (1) expands considering the penalty method:

$$(\boldsymbol{K} + \beta \boldsymbol{G}^T \boldsymbol{G})\boldsymbol{u} + \boldsymbol{M}\ddot{\boldsymbol{u}} = \boldsymbol{f} + \beta \boldsymbol{G}^T \boldsymbol{v} \tag{8}$$

and the perturbed Lagrangian formulation:

$$\begin{bmatrix} \boldsymbol{K} & \boldsymbol{G}^T \\ \boldsymbol{G} & -{}^{1}\!/_{\beta}\,\boldsymbol{I} \end{bmatrix} \begin{bmatrix} \boldsymbol{u} \\ \boldsymbol{\lambda} \end{bmatrix} + \begin{bmatrix} \boldsymbol{M} & \boldsymbol{0} \\ \boldsymbol{0} & \boldsymbol{0} \end{bmatrix} \begin{bmatrix} \ddot{\boldsymbol{u}} \\ \boldsymbol{0} \end{bmatrix} = \begin{bmatrix} \boldsymbol{f} \\ \boldsymbol{v} \end{bmatrix} \tag{9}$$

In this context, the Lagrange multipliers $\boldsymbol{\lambda}$ can be interpreted as a contact force [5]. In principle, the time derivative of the Lagrange multiplier $\ddot{\boldsymbol{\lambda}}$ can additionally extend Eq. (9) if contact conditions are added to the mass matrix and acceleration vector. According to Wissmann and Sarnes [17], a disadvantage here is that very small or large eigenvalues result from additional constraints. For this reason, only the stiffness matrix and the displacements vector contain contact conditions according to Eq. (7) in our paper.

The penalty parameter β can be understood as a numerical contact stiffness [4]. In the case of bonded contact, identical values for the contact stiffness parameter for normal and tangential directions are typically chosen [9]. Recommendations from the literature provide appropriate values for static contact problems. These parameter proposals are listed in Table I with the corresponding reference. Thus, the contact stiffness parameters rely on the maximal stiffness matrix diagonal entry $max(K_{ii})$ or the minimal matrix value K_{min} being involved in constraints. Further, some contact stiffnesses can depend on the machine's accuracy t^z, or the word length $d = 16$, which describes the number of decimals. Following [13], even the model size becomes crucial with regard to the number of degrees of freedom n_{dof}.

Table I: Recommendations from the literature for β and input parameters of the use case.

Contact stiffness β [-]	**Literature references**	**Model parameter** [unit]	**Value**
$\gg max(K_{ii})$	Bathe [5]	Density [$t \cdot mm^{-3}$]	$7.85 \cdot 10^{-9}$
$\approx 10^{2 \ldots 4} \cdot max(K_{ii})$	Rust [10]	Poisson's ratio [-]	0.3
$\leq \frac{\lvert K_{min} \rvert}{\sqrt{n_{dof} \cdot t^z}}$	Wriggers [13]	Young's modulus [$N \cdot mm^{-2}$]	210,000
		Degrees of freedom n_{dof} [-]	176,820
$\leq 10^{\frac{d}{2}}$	Cook et al. [15] Wissmann and Sarnes [17]	$max(K_{ii})$ [-]	$3.5245 \cdot 10^{7}$
		$\lvert K_{min} \rvert$ [-]	$8.5837 \cdot 10^{1}$
$= max(K_{ii}) \cdot 10^4$	Chandrupatla and Belegundu [19]	Machine accuracy t^z[-]	$2.2204 \cdot 10^{-16}$

The concrete model parameters as well as further necessary information for the numerical modal analysis are provided in Table I. The resulting contact stiffness values are evaluated concerning the modal analysis. We use both contact formulations Eqs. (8) and (9) and obtain the generalized eigenvalue problems for the penalty method:

$$\left((\boldsymbol{K} + \beta \boldsymbol{G}^T \boldsymbol{G}) - \boldsymbol{\Lambda} \boldsymbol{M}\right) \boldsymbol{\Phi} = \boldsymbol{0} \tag{10}$$

and the perturbed Lagrangian formulation:

$$\left(\begin{bmatrix} \boldsymbol{K} & \boldsymbol{G}^T \\ \boldsymbol{G} & -{}^{1}\!/_{\beta}\,\boldsymbol{I} \end{bmatrix} - \boldsymbol{\Lambda} \begin{bmatrix} \boldsymbol{M} & \boldsymbol{0} \\ \boldsymbol{0} & \boldsymbol{0} \end{bmatrix} \right) \boldsymbol{\Phi} = \boldsymbol{0} \tag{11}$$

The matrix dimension is not going to be enlarged by the penalty method. Nevertheless, contact constraint equations may fill in previously empty entries of the system stiffness matrix. Due to perturbed Lagrange-procedure, additional degrees of freedom of the constraints matrix $\boldsymbol{G}$ expand the system stiffness matrix. However, they do not modify the unconstrained stiffness entries so that a sparse structure remains. Besides, the perturbed Lagrange-method can be transformed to the penalty method by eliminating the Lagrange multipliers $\boldsymbol{\lambda}$. With $\beta \rightarrow \infty$, the original Lagrange procedure is approximated [17]. However, as a disadvantage of large parameters β overconstraints and ill-conditioning could lead to numerical instabilities [10].

The constrained eigenproblems in Eqs. (10) and (11) can be solved by using the implicitly restarted Arnoldi method in Eqs. (5) and (6). An essential assumption within the linear dynamics problems is that each contact state persists starting from the base state [20]. This means for the present application example of a non-matching FE mesh, each ideal bonded contact is preserved and does not open or change during the very short calculation time.

3. EXPERIMENTAL VERIFICATION

The results of an experimental measurement verify the investigated contact simulations as a reference solution (see Fig. 2). The ideal bonded contact of the FEA can be interpreted in its elastic behaviour as a single part. For this particular case, the single part of flat steel (90MnCrV8) is considered without contact in the experiment to verify the simulations.

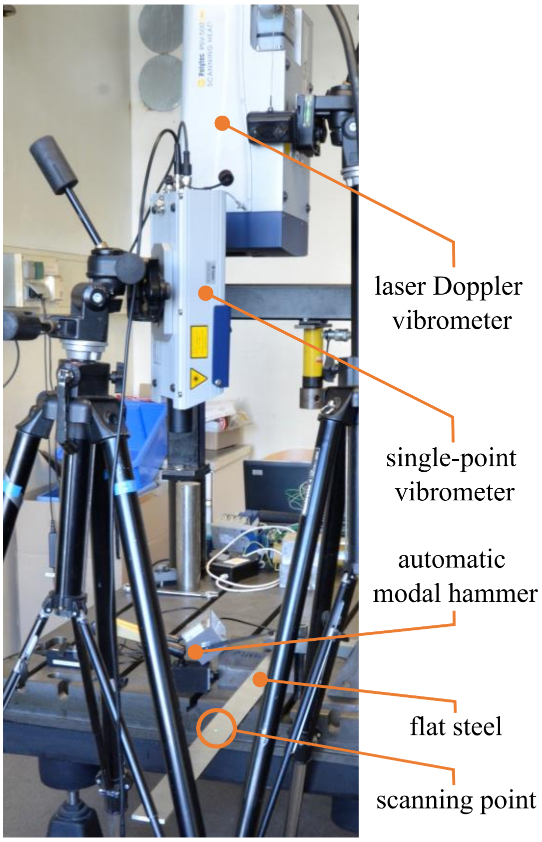

Figure 2: Experimental set-up of the flat steel specimen.

The scanning laser Doppler vibrometry employed is based on the optical interferometry principle by using the Doppler effect [21]. Therefore, it states that light waves undergo a motion-dependent change in their oscillation frequency when scattering from moving specimen surfaces [21]. The frequency change resulting from this is directly proportional to the instantaneous value of the oscillation velocity [22]. To provide a correct reference to the laser scanning points measured one after the other, the single-point vibrometer takes an additional phase reference of the flat steel. Figs. 2 and 3 present the specimen with the set-up that is necessary to measure natural frequencies and corresponding mode shapes. At one end side, the sample flat steel is clamped in both the experiment and the FE model ($u_{x,y,z}= 0$). Consequently, the dimensions of the specimen's free side are 800 mm × 50 mm × 6 mm. Fig. 3 displays a detailed view of the flat steel with the applied boundary conditions counting the clamping restraint.

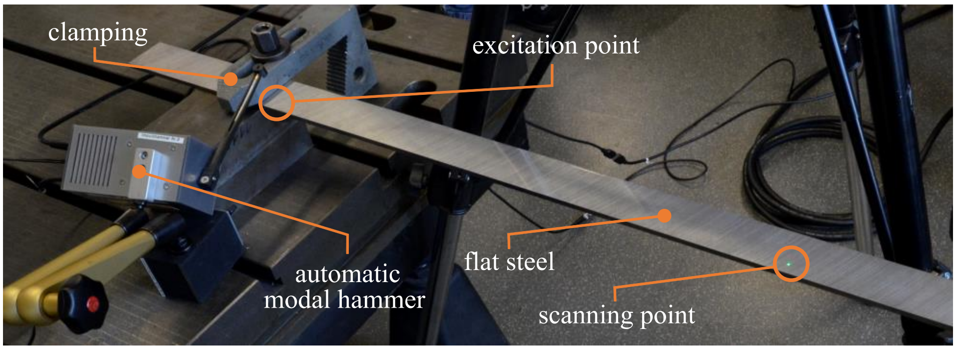

Figure 3: Clamped flat steel excited by the automatic modal hammer.

To obtain natural vibrations, a scalable automatic modal hammer excites the specimen with a repeatable force level and without any mass-loading. During the experiment, each excitation is conducted with an identical impulse at a constant point near to the clamped end (see Fig. 3). Velocities created through one excitation are measured directly via the laser Doppler vibrometer (see Fig. 2) [23]. This procedure is carried out for each individual laser scanning point. In our study, an area discretization consisting of 210 scanning points is performed for the measurement. The velocities optically measured at the scanning points are analysed using fast Fourier transform (FFT) and are additionally transformed into deflections (see Fig. 4) [23]. Consequently, the natural frequencies of the flat steel sample are approximated by the sum of all velocity amplitude responses.

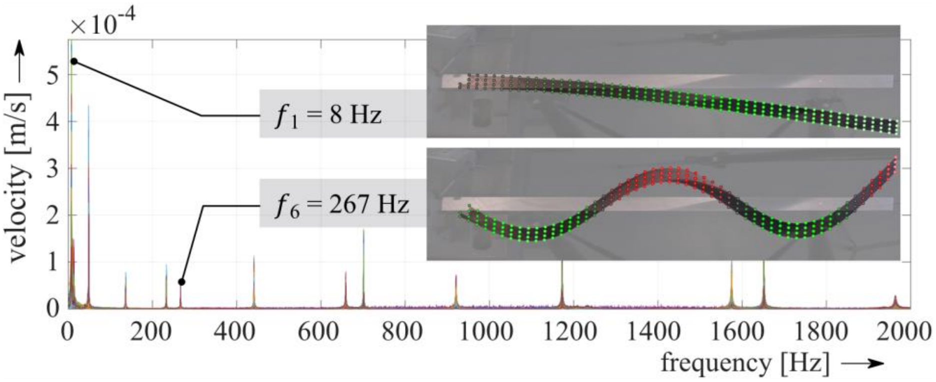

Figure 4: Frequency response function of the specimen with two corresponding mode shapes.

As Fig. 4 shows, the measured natural frequencies are located at the concentrated peaks of the response functions. In order to classify the first and sixth natural frequencies more clearly, the corresponding mode shapes resulting from the measurements are added to Fig. 4. These represent the bending vibration modes φ_1 and φ_6 by evaluating the deflection amplitudes of each scanning point using the data acquisition system from Polytec GmbH [23]. The recorded phase reference allows the sequentially measured data from both vibrometers to be correlated in the correct phase for vibration animation. The positioning of the highly precise vibrometer determines the measurement uncertainty, as the instantaneous value of the vibration velocity in the beam direction influences the Doppler frequency shift [22]. Our measurements attempted an ideally aligned scanning head at an angle of 90° between the laser beam direction and the point grid of the flat steel surface, see Fig. 2. Deviations of up to 8° would cause a frequency deviation error of about 1 % [23].

The experimentally obtained vibrations can now be provided in the further procedure for a verification of the simulations. A comparable investigation of finite-element and experimental modal analysis of a flat steel with similar natural frequencies is mentioned in the literature [24]. However, the measurement of the free vibration behaviour by [24] is carried out tactilely by attaching an accelerometer to the free end of the cantilever structure. For the sample in our paper no additional sensor mass is applied because an optical measuring technology is used. This ensures an exact verification of the simulation. The reference contribution [24] did not examine a bonded contact model in the simulation, but one solid with a matching FE mesh. In contrast, a non-matching mesh is investigated in the numerical modal analysis of our contribution. This non-matching mesh is needed to identify a conclusion about the influence of the contact stiffness on the modal analysis results. The bonded contact model concerning the non-matching, locally refined mesh is visualized in Fig. 5. The mesh remained unchanged during our parameter study. For the location of the analysed contact zone the middle in thickness direction is used. This represents a particular case, since the elastic behaviour of master and slave are identical with the same dimensions. To ensure comparability between the measurement and simulation, the specimen, master and slave have identical material properties (see Table I).

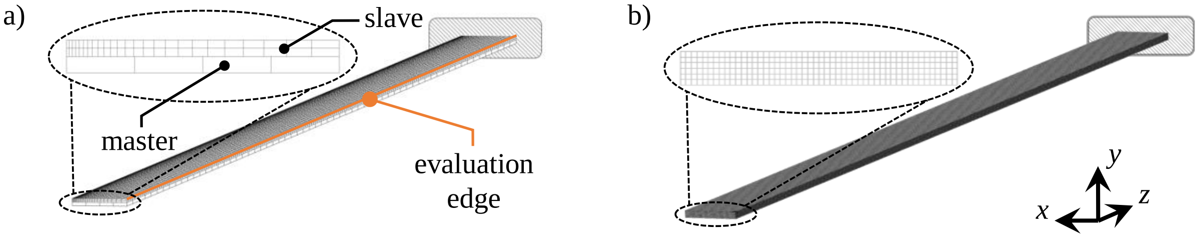

Figure 5: FE models, a) locally refined mesh with contact zone, b) globally fine reference mesh.

Due to the complexity of comparing mode shapes or eigenvectors φ_i, there are many approaches to fix a measure of agreement. For example, a scalar value between 0 and 1 can classify the correspondence of two eigenvectors via the modal assurance criterion [25, 26]. The main disadvantage herein is that an exact course of one mode shape cannot be observed. For this reason, a nodal edge on the top of the slave body is evaluated in this contribution (see Fig. 5). To compare the mode shapes of the simulations and measurement, a detailed contrast of the investigations is made based on the displacements in y direction at the z coordinates. The mode shapes are displacement-normalized for each eigenvector of the whole structure [27].

4. RESULTS AND DISCUSSION

As the contact stiffness is known to influence the accuracy of the simulation results of modal analyses, an appropriate contact stiffness parameter β is needed to obtain valid natural frequencies and mode shapes. Therefore, a parameter study is required in which the contact settings are varied. Node-to-Segment and Gauss-Point-to-Segment (GPTS) at 16 Gauss Points are applied for the contact discretization approach. Furthermore, both contact formulations Penalty and perturbed Lagrange method are compared. For each contact setting, the contact stiffness parameter is varied within the range of $10^0 \leq \beta \leq 10^{16}$, with a total of 48 steps evenly distributed on a logarithmic scale. In the following, the first six natural frequencies and corresponding eigenvectors are investigated (see Table II), which include the first relevant bending and torsional vibrations in the different spatial directions [27].

Figs. 6 and 7 show each a detailed plot of the calculated natural frequency versus contact stiffness β for the first and the sixth vibration mode. In both cases, a stable plateau for the natural eigenfrequencies is obtained, indicating the range of suitable contact settings. Suitable contact parameters can be identified quantitatively by comparing the natural frequency results of the FE mesh models with and without contact zone, see Fig. 5. A relative discrepancy between the natural frequencies of $|\Delta f_i| \leq 1$ % is used as a criterion for a valid β. All those suitable contact stiffness parameters are compared in Table II for the results of f_1 to f_6.

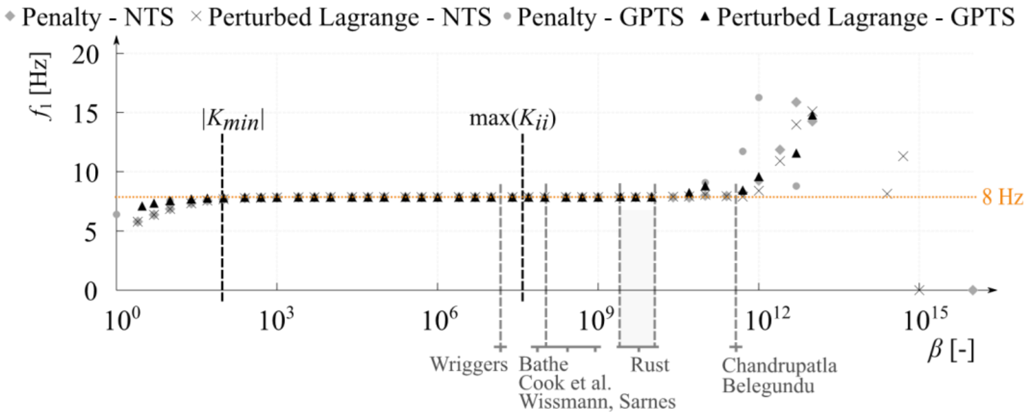

Figure 6: First natural frequency f_1 at the investigated contact stiffness parameters.

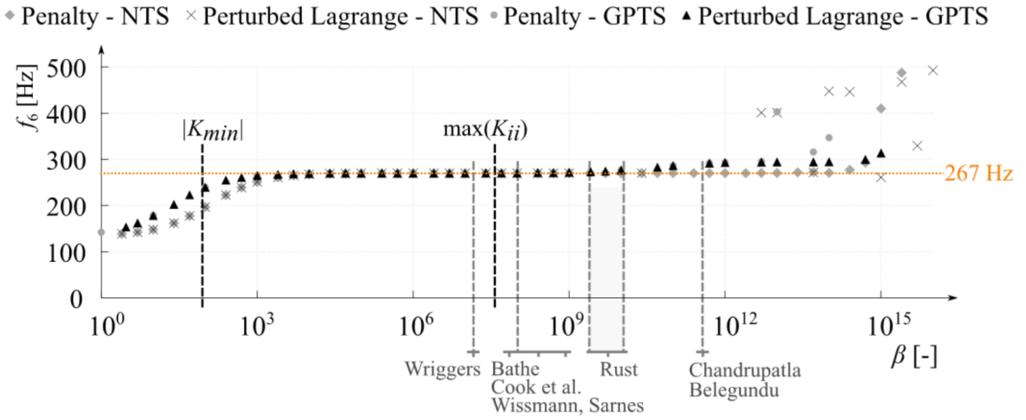

Figure 7: Sixth natural frequency f_6 at the investigated contact stiffness parameters.

Table II: Correct parameters β for the first six natural frequencies f_i of the flat steel sample.

Imposition method	**Perturbed Lagrange**		**Penalty**		**Associated mode shape**
Contact discretization	**NTS**	**GPTS**	**NTS**	**GPTS**	
$\beta(f_1)$	$5.0\cdot10^2\ldots5.0\cdot10^{10}$	$1.0\cdot10^2\ldots1.0\cdot10^{10}$	$5.0\cdot10^2\ldots5.0\cdot10^{10}$	$1.0\cdot10^2\ldots1.0\cdot10^{10}$	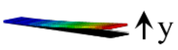
$\beta(f_2)$	$2.5\cdot10^3\ldots1.0\cdot10^9$	$5.0\cdot10^2\ldots1.0\cdot10^{10}$	$2.5\cdot10^3\ldots1.0\cdot10^{12}$	$1.0\cdot10^3\ldots1.0\cdot10^{10}$	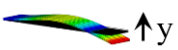
$\beta(f_3)$	$2.5\cdot10^0\ldots1.0\cdot10^9$	$2.5\cdot10^0\ldots1.0\cdot10^{13}$	$2.5\cdot10^0\ldots1.0\cdot10^{12}$	$1.0\cdot10^0\ldots1.0\cdot10^{11}$	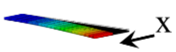
$\beta(f_4)$	$1.0\cdot10^4\ldots1.0\cdot10^9$	$5.0\cdot10^3\ldots5.0\cdot10^9$	$1.0\cdot10^4\ldots1.0\cdot10^{13}$	$1.0\cdot10^4\ldots1.0\cdot10^9$	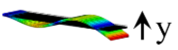
$\beta(f_5)$	$2.5\cdot10^5\ldots1.0\cdot10^9$	$5.0\cdot10^4\ldots1.0\cdot10^{12}$	$2.5\cdot10^5\ldots1.0\cdot10^{13}$	$1.0\cdot10^5\ldots5.0\cdot10^{11}$	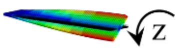
$\beta(f_6)$	$1.0\cdot10^4\ldots1.0\cdot10^9$	$5.0\cdot10^3\ldots1.0\cdot10^9$	$1.0\cdot10^4\ldots1.0\cdot10^{14}$	$1.0\cdot10^4\ldots1.0\cdot10^9$	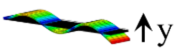

The comparison confirms that a choice of β within the plateau region leads to the correct natural frequencies. Furthermore, the diagrams above confirm a deviation from the correct natural frequency seen for very small and high β. Nearly all of the investigated natural frequencies (with exception of f_3, compare Table II) tend to decrease in magnitude at low contact stiffnesses. In contrast, too high parameters lead to increased natural frequencies or even to solver abort. Further aspects that are observed from this parameter variation follow.

In particular the perturbed Lagrange method diverges for $\beta > 10^9$ with the NTS contact discretization for higher frequency orders. It computes only partial solutions, that means for instance only at the first natural frequency (see Fig. 6). Higher order natural frequencies (see f_6 in Fig. 7 and Table II) cannot be determined, which indicates a numerical problem.

The calculations with the GPTS contact discretization already provide suitable natural frequencies at slightly smaller contact stiffnesses β than with the NTS contact discretization.

The plateau region shifts a little along the β axis depending on the eigenmode. Even very small values for the contact stiffness are permissible for calculating the third natural frequency, see Table II. The smaller the value of β, the more elastic the bonded contact, which may lead to a (small) relative motion of the contact pair. But this effect will only occur if the flat steel vibrates in the specific eigenmode, so there would be noticeable tension on the bonded contact. If the flat steel vibrates in a specific eigenmode like e.g. the first bending mode at f_1, the tension in the bonded contact zone would be higher. Consequently, the influence of the contact stiffness would be more decisive on this natural frequency. The third mode shape is a bending mode in the x direction (so-called in-plane [27]), which is why no significant tensions occur in the bonded contact. Therefore, very small contact stiffnesses are suitable.

Commonly, a reduction of the natural frequency value occurs for very low β. A reason could be the separation or penetration of the contact zone between master and slave body due to insufficient contact stiffness. However, if the contact stiffness is too high, numerical challenges arise. Firstly, this leads to artificially stiffened structural behaviour with consequently increased natural frequencies. Secondly, the calculation may fail to find an eigensolution and therefore aborts. Randomly occurring natural frequencies are a consequence of ill-conditioning of the system matrix.

Furthermore, Figs. 6 and 7 present the proposed values from the criteria stated in the literature. In addition, $max(K_{ii})$ and the smallest stiffness value $|K_{min}|$, that is modified by β due to imposing constraints, are identified. So far, applied criteria according to the references in Table I are not entirely suitable considering the stiffness in the contact zone. According to [10, 19], findings can only be transferred to modal analysis to a limited extent. The contact stiffness parameters following [5, 13, 15, 17] provide correct natural frequencies for the bonded contact flat steel model. Interpreting these findings in Figs. 6 and 7, a range of smaller β is already useful, which is not obtained from the literature. On this basis, we conclude that absolute contact stiffnesses of 10^5 to 10^9 lead to correct natural frequencies considering bonded contact in the modal analysis of the flat steel sample. This estimation for suitable contact stiffness values applies to higher natural frequencies not shown here. A necessary prerequisite for this is an unchanged structural stiffness, machine accuracy, and problem size. The mode shape $\boldsymbol{\varphi}_6$ in Fig. 8 a shows the influence of an overlarge contact stiffness on the modal analysis results in terms of the total displacements.

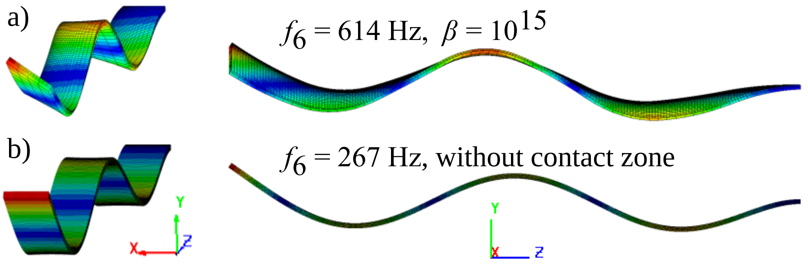

Figure 8: Sixth mode shape $\boldsymbol{\varphi}_6$ of the a) non-matching contact model with very high contact stiffness, b) single part model with globally constant mesh size.

Consequently, an asymmetrical bending vibration amplitude will occur due to an excessively global high contact stiffness in combination to the locally refined, non-matching mesh (Fig. 5). In comparison, the FE model of a structured fine matching mesh without the need of a contact zone is simulated (Fig. 8 b); mesh size: 1 mm; 240,000 elements of twenty-node hexahedrons). It provides a correct mode shape from the FEM in addition to the experimental solution in Fig. 4. The deviation of the natural frequencies in terms of magnitude is moreover a clear indication of an excessive contact stiffness (Fig. 9).

In order to compare the simulations even more to reality, displacement-normalized mode shapes from EMA are illustrated for the first and sixth mode shapes $\boldsymbol{\varphi}_1$ and $\boldsymbol{\varphi}_6$ in Fig. 9.

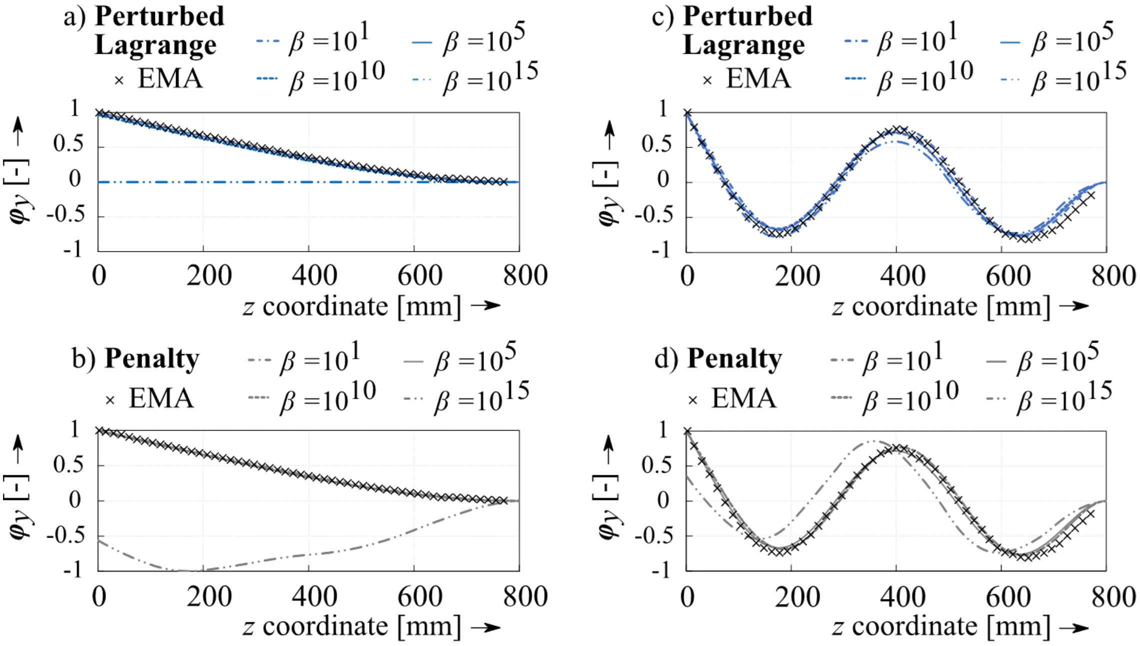

Figure 9: Displacements in y direction of the first mode shape $\boldsymbol{\varphi}_1$ for a) perturbed Lagrange-, b) penalty-formulations and of the sixth mode shape $\boldsymbol{\varphi}_6$ for c) perturbed Lagrange-, d) penalty-formulations.

Thereby, these are compared with the simulation displacements in y direction. Herein, the surface-based contact discretization (GPTS) is executed for four selected β with perturbed Lagrange and penalty method. Fig. 9 indicates the displacement-normalized mode shapes at low and high β along the evaluation edge of the flat steel (see Fig. 5). Both perturbed Lagrange- and the penalty method deliver accurate mode shape results for $\beta = 10^1$ to 10^{10} at the fundamental frequency in y direction f_1 in Figs. 9 a and 9 b. If the contact stiffness setting is too large, for instance $\beta = 10^{15}$, the structural response will behave incorrectly. In the same way Figs. 9 c and 9 d show the normalized deformation curve of the sixth natural frequency f_6. Analogous to the first mode shape, results for $\beta = 10^1$ to 10^{10} are recorded nearly consistent with those from the EMA. The very high contact stiffness parameter $\beta = 10^{15}$ leads to a reduction of the deformation amplitude at $z = 400$ mm considering the perturbed Lagrange-method. The relative deviation at this point is about 17 %. Furthermore, a left shift of the mode shape with additional amplitude errors occurs when $\beta = 10^{15}$ is accounted for in the penalty method. With regard to the low contact stiffness parameters $\beta = 10^1$, no clear conclusion can be drawn about the normalized vibration shapes $\boldsymbol{\varphi}_1$ and $\boldsymbol{\varphi}_6$. In that case, the displacements in y direction show the same curve as with a suitable contact stiffness regardless of whether the contact is bonded or separated. In general, the influence of the contact stiffness on the natural frequencies can be seen to be significantly stronger than on the associated mode shape through the test evaluation demonstrated. The reason is that with the strongly deviating natural frequencies of the observed cases, only low changes in the mode shape appear in comparison to the correct reference solution. Although the natural frequencies receive erroneous values for the parameters $\beta > 10^9$, mode shape curves of $\beta = 10^{10}$ provide close matches.

5. CONCLUSION

Computational contact dynamics is commonly considered for modal analysis in a linear base state, which remains closed in our case. Suitable contact stiffnesses are needed for the bonded finite element problems to avoid errors from the contact settings. Therefore, we aimed to visualize the notable influence of contact constraints on the natural frequencies and corresponding mode shapes. The simulation results of a clamped flat steel specimen have been verified against an experimental modal analysis. In this way, suitable ranges for β in the modal analysis have been identified. Especially the penalty method with Node-to-Segment contact discretization provided a wide range of suitable contact stiffnesses in our research. Thus, the modal analysis does not necessarily require more elaborate approaches, such as double penalization of the mass and stiffness matrices. That confirmed the thesis of Wissmann and Sarnes [17], and Glenk [18], which state that imposing contact constraints only on the stiffness force leads to correct results in the modal analysis.

Furthermore, the contact stiffness recommendations known from the literature were applied to the modal analysis. In general, the recommendations for contact stiffness values according to Bathe [5], Wissmann and Sarnes [17], and Cook et al. [15] provide correct results for the first six natural frequencies investigated. Based on our study, the criterion recommended by Wriggers [13] provides the best prediction for adequate contact stiffness. According to him, the parameter β depends on the smallest stiffness value changed by the imposition of constraints, the machine accuracy and the problem size. The other criteria mentioned occur too stiff in all calculations and promote too high natural frequencies or even a solver abortion.

Moreover, our study showed that the influence of the unsuitable contact stiffness on the natural frequencies is significantly stronger than on the associated mode shapes.

Overall, we conclude that values of the contact stiffness β lower (by a factor of about 100) than recommended by usual criteria are generally well suited for modal analyses.

Further research will address the determination of a local contact stiffness parameter as a function of element size and material stiffness when considering non-matching, locally refined meshes in modal analyses. The simulative and experimental investigation complexity could be increased using the example of a gearbox contact.

ACKNOWLEDGEMENT

We would like to thank Polytec GmbH for the possibility of carrying out experimental tests. Partly funded by the Deutsche Forschungsgemeinschaft (DFG, German Research Foundation – 491183248) / Open Access Publishing Fund of the University of Bayreuth. Partly funded by the European Social Fund (ESF) and the Oberfrankenstiftung within the project OpAL (StMBW-W-IX.4-6-210091).

REFERENCES

[1] Poklemba, R.; Duplakova, D.; Zajac, J.; Duplak, J.; Simkulet, V.; Goldyniak, D. (2020). Design and investigation of machine tool bed based on polymer concrete mixture, *International Journal of Simulation Modelling*, Vol. 19, No. 2, 291-302, doi:10.2507/IJSIMM19-2-518

[2] Sampayo, D.; Luque, P.; Mantaras, D. A.; Rodriguez, E. (2021). Go-kart chassis design using finite element analysis and multibody dynamic simulation, *International Journal of Simulation Modelling*, Vol. 20, No. 2, 267-278, doi:10.2507/IJSIMM20-2-555

[3] Tonazzi, D.; Massi, F.; Salipante, M.; Baillet, L.; Berthier, Y. (2019). Estimation of the normal contact stiffness for frictional interface in sticking and sliding conditions, *Lubricants*, Vol. 7, No. 7, Paper 56, 17 pages, doi:10.3390/lubricants7070056

[4] Billenstein, D.; Glenk, C.; Diwisch, P.; Rieg, F. (2018). Investigation of contact settings on the result of topology optimization to avoid contact stiffness supports, Schumacher, A.; Vietor, T.;

Fiebig, S.; Bletzinger, K. U.; Maute, K. (Eds.), *Advances in Structural and Multidisciplinary Optimization*, Springer, Cham, 1455-1467, doi:10.1007/978-3-319-67988-4_110

[5] Bathe, K.-J. (2014). *Finite Element Procedures*, 2nd edition, Klaus-Jürgen Bathe, Watertown

[6] Rieg, F.; Hackenschmidt, R.; Alber-Laukant, B. (2014). *Finite Element Analysis for Engineers: Basics and Practical Applications with Z88Aurora*, Hanser Publications, Munich

[7] Huebner, K. H.; Dewhirst, D. L.; Smith, D. E.; Byrom, T. G. (2001). *The Finite Element Method for Engineers*, 4th edition, John Wiley & Sons, Hoboken

[8] Lehoucq, R. B.; Sorensen, D. C.; Yang, C. (1998). *ARPACK Users' Guide: Solution of Large-scale Eigenvalue Problems with Implicitly Restarted Arnoldi Methods*, Society for Industrial and Applied Mathematics, Philadelphia

[9] Nützel, F. (2015). *Entwicklung und Anwendung eines Finite-Elemente-Systems auf Basis von Z88 zur Berechnung von Kontaktaufgaben aus der Antriebstechnik*, PhD Thesis, Universität Bayreuth, Bayreuth (in German)

[10] Rust, W. (2015). *Non-Linear Finite Element Analysis in Structural Mechanics*, Springer, Cham, doi:10.1007/978-3-319-13380-5

[11] De Lorenzis, L.; Wriggers, P.; Zavarise, G. (2012). A mortar formulation for 3D large deformation contact using NURBS-based isogeometric analysis and the augmented Lagrangian method, *Computational Mechanics*, Vol. 49, No. 1, 1-20, doi:10.1007/s00466-011-0623-4

[12] Konyukhov, A.; Schweizerhof, K. (2013). *Computational Contact Mechanics: Geometrically Exact Theory for Arbitrary Shaped Bodies*, Springer-Verlag, Berlin

[13] Wriggers, P. (2006). *Computational Contact Mechanics*, 2nd edition, Springer-Verlag, Berlin

[14] Wagner, M. (2017). *Lineare und Nichtlineare FEM*, Springer, Wiesbaden

[15] Cook, R. D.; Malkus, D. S.; Plesha, M. E.; Witt, R. J. (2001). *Concepts and Applications of Finite Element Analysis*, 4th edition, Wiley, Madison

[16] Hetherington, J.; Rodríguez-Ferran, A.; Askes, H. (2012). The bipenalty method for arbitrary multipoint constraints, *International Journal for Numerical Methods in Engineering*, Vol. 93, No. 5, 465-482, doi:10.1002/NME.4389

[17] Wissmann, J.; Sarnes, K.-D. (2006). *Finite Elemente in der Strukturmechanik*, Springer, Heidelberg, doi:10.1007/3-540-29277-2

[18] Glenk, C. (2020). *Strukturdynamische Finite-Elemente-Analyse im Kontext der Antriebstechnik*, Shaker Verlag, Düren

[19] Chandrupatla, T. R.; Belegundu, A. D. (2002). *Introduction to Finite Elements in Engineering*, 3rd edition, Pearson, Hoboken

[20] Dassault Systemes. Abaqus Analysis User's Guide, from *http://130.149.89.49:2080/v6.14/books/usb/default.htm*, accessed on 05-09-2022

[21] Santulli, C.; Jeronimidis, G. (2006). Development of a method for nondestructive testing of fruits using scanning laser vibrometry, *e-Journal of Nondestructive Testing*, Vol. 11, No. 10, Paper 10, 12 pages

[22] Marschner, H.; Reckwerth, D.; Steger, H. (2008). Innovative Schwingungsmesstechnik in der Bremsenentwicklung, ATZ – *Automobiltechnische Zeitschrift*, Vol. 110, No. 2, 128-136, doi:10.1007/BF03221954

[23] Polytec GmbH. PSV, from *https://www.polytec.com*, accessed on 13-10-2021

[24] Chaphalkar, S. P.; Khetre, S. N.; Meshram, A. M. (2015). Modal analysis of cantilever beam structure using finite element analysis and experimental analysis, *American Journal of Engineering Research*, Vol. 4, No. 10, 178-185

[25] Allemang, R. J. (2003). The modal assurance criterion: twenty years of use and abuse, *Sound and Vibration*, Vol. 37, No. 8, 14-23

[26] Greś, S.; Döhler, M.; Mevel, L. (2021). Uncertainty quantification of the modal assurance criterion in operational modal analysis, *Mechanical Systems and Signal Processing*, Vol. 152, Paper 107457, 21 pages, doi:10.1016/j.ymssp.2020.107457

[27] Abbey, T. (2018). *How to Perform Linear Dynamics Analysis*, NAFEMS Ltd, Hamilton